American Mineralogist, Volume 104, pages 1131–1142, 2019

Solving the iron quantification problem in low-kV EPMA: An essential step toward improved analytical spatial resolution in electron probe microanalysis—Olivines

AURÉLIEN MOY[1,*], JOHN H. FOURNELLE[1], AND ANETTE VON DER HANDT[2]

[1]Department of Geoscience, University of Wisconsin, Madison, Wisconsin 53706, U.S.A.
[2]Department of Earth Sciences, University of Minnesota, Minneapolis, Minnesota 55455, U.S.A.

ABSTRACT

The relatively recent entry of field emission electron microprobes into the field of microanalysis provides another tool for the study of small features of interest (e.g., mineral and melt inclusions, exsolution lamellae, grain boundary phases, high-pressure experimental charges). However, the critical limitation for accurate quantitative analysis of these submicrometer- to micrometer-sized features is the relationship between electron beam potential and electron scattering within the sample. To achieve submicrometer analytical volumes from which X-rays are generated, the beam accelerating voltage must be reduced from 15–20 to ≤10 kV (often 5 to 7 kV) to reduce the electron interaction volume from ~3 to ~0.5 μm in common geological materials. At these low voltages, critical *K*α X-ray lines of transition elements such as Fe are no longer generated, so *L* X-ray lines must be used. However, applying the necessary matrix corrections to these *L* lines is complicated by bonding and chemical peak shifts for soft X-ray transitions such as those producing the Fe*L*α X-ray line. It is therefore extremely challenging to produce accurate values for Fe concentration with this approach. Two solutions have been suggested, both with limitations. We introduce here a new, simple, and accurate solution to this problem, using the common mineral olivine as an example. We also introduce, for the first time, olivine results from a new analytical device, the Extended Range Soft X-ray Emission Spectrometer.

Keywords: EPMA, olivine, low-kV, iron, microprobe, SXES, EMPA

INTRODUCTION

The electron probe microanalyzer (a.k.a., electron microprobe) has been an invaluable tool for Earth and planetary science since 1958, when its inventor Raimond Castaing and researcher Fredriksson (1958) determined that tiny (<60 μm) spherules found in deep-sea sediments were in fact extraterrestrial, by matching spherule compositions to the unique Fe:Ni signature of iron meteorites. Over the intervening five decades, the electron microprobe has been essential in virtually every aspect of geochemistry, mineralogy, and petrology of both terrestrial and extraterrestrial materials.

Electron microscopes and microprobes traditionally have used bent tungsten wire filaments as their beam source (and occasionally LaB_6). Over the past decades, many scanning electron microscopes (SEM) and transmission electron microscopes (TEM) have switched to cold field emission (FE) gun beam sources. These FE electron sources provide brighter beams (smaller diameter, higher electron flux) relative to the traditional sources (Vladár and Postek 2009), making images from FE SEMs significantly sharper and providing higher spatial resolution images. However, the long-term instability of cold-emission sources makes them inadequate for the demands of quantitative analysis. The advent of thermal Schottky emission-type sources, which facilitate similarly small beam diameters but are more stable, represents a key advance that enables not only equivalent imaging to FE SEMs but higher spatial resolution quantitative analysis than traditional electron microprobes.

An example is given in Figure 1, where a secondary electron image (SEI) of an iron oxide crystal in NIST glass K409 (described in Fournelle et al. 2016) was taken with a JEOL JXA-8530FPlus electron microprobe. Here, the beam diameter can be determined using the edge resolution technique as described by Barkshire et al. (2000): the beam diameter corresponds to the distance over which some percentage change in signal intensity occurs in a scan over a sharp edge between two features. For the line crossing the interface in Figure 1a, the associated image intensity values are given in Figure 1b. Optimally, the adjacent dark and bright areas are "flat." However, in reality there are edge effects in many instances, so an error function is fit to normalize each of the darker and brighter regions. Traditionally, the image resolution or "beam diameter," is defined as the distance over which there is a signal rise from either 10 to 90%, 16 to 84%, or 25 to 75%. Following this convention, the beam diameter could be defined correspondingly as 38, 58, or 72 nm. Current usage seems to prefer the intermediate 16–84% rise (International Organization for Standardization 2003).

However, even if electron images can be acquired with 10 to hundreds of nanometer spatial resolution, the fact that an electron beam is generated by a field emission source does not change the fundamental physical processes by which electrons are scattered within the specimen and from which X-rays are generated. Indeed, to accurately probe small features, e.g., small inclusions, it is important to have a good estimate of the X-ray

---

* E-mail: amoy6@wisc.edu

0003-004X/19/0008–1131$05.00/DOI: https://doi.org/10.2138/am-2019-6865

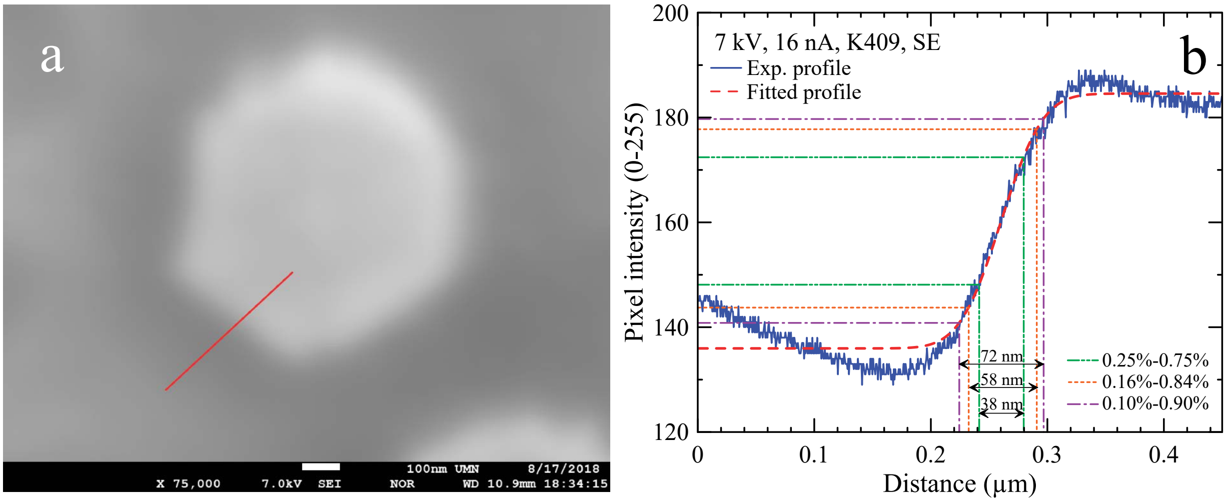

FIGURE 1. (**a**) SE image of an 800 nm iron oxide crystal in K409 silicate glass. A profile is drawn across a crystal edge to calculate the "edge resolution" based on the change in signal intensity. (**b**) Edge resolution, determined by fitting the signal intensity profile with an error function. Depending upon the preferred convention of the degree of relative intensity change, various beam diameters may be calculated.

lateral resolution achievable. This concept is not only governed by the beam size but also the electron ionization range, through the beam potential.

Typically, although not exclusively, Earth science researchers operate electron microprobes at gun voltages of 15 kV[1] for silicates, carbonates, phosphates, etc., and 20 kV for sulfides (and either voltage for metal oxides). These electron beam voltages result in electron scattering interaction volumes on the order of 2 to 3 μm, with the primary X-rays generated within these volumes being much too large for many small features of interest.

MONTE CARLO MODELING OF X-RAY GENERATION

To estimate the X-ray lateral resolution in addition to the beam diameter, the electron ionization range must be estimated. Analytical expressions aimed at calculating this electron ionization range were developed since the beginning of the electron microprobe era (Castaing 1960; Duncumb 1960; Anderson and Hasler 1966; Reed 1966) up to recently (Hovington et al. 1997b; Merlet and Llovet 2012). However, Fournelle et al. (2016) showed that these models have limitations, especially for low accelerating voltages.

Another approach to estimating X-ray lateral resolution is to create a Monte Carlo simulation, wherein a large number of "random walks" of high energy electrons impinge upon and penetrate a specified material of a given geometry, and the occurring physical processes (e.g., elastic and inelastic scattering, inner shell ionization, photoelectric absorption) are included in the computer codes. The speed of the simulation scales with the degree of simplification and approximation utilized. Three freely available programs of note are CASINO (Hovington et al. 1997a), DTSA-II (Ritchie 2011), and PENEPMA/PENELOPE (Salvat et al. 2013; Llovet and Salvat 2016). Many microanalysts utilize these simulations to estimate the interaction volume for particularly small-sized features of interest prior to setting the appropriate beam energy for EPMA operation.

The Monte Carlo simulation shown in Figure 2 illustrates that the electron beam energy is the primary factor in determining the size of the zone where X-rays are produced, not the electron beam source whether it be tungsten, LaB_6 or field emission source. The outer contour represents where the generation of Mg*K*α X-rays in an Fo_{80} olivine is only 1% of the maximum produced intensity from a 15 kV source. This contour is only slightly smaller for the field emission source, slightly less than 2 μm laterally, compared to approximately 2.2 μm laterally for the tungsten source—the difference being approximately equal to the proportional difference in beam diameters (under the general assumption that the electron beam has a Gaussian distribution). It is worth noting that Figure 2 only describes the generation of the Mg*K*α X-rays and does not take matrix absorption effects into consideration. Indeed, because of the absorption of the X-rays leaving the sample, the emitted X-ray generation volume will be slightly different from the generated X-ray production (or ionization range) volume.

Fournelle et al. (2016) showed that estimates of the ionization range by Monte Carlo simulation programs (in particular PENEPMA) matched those of experiments well when using a limited set of experimental data at 5 and 7 kV. This corroborates the usefulness of the Monte Carlo simulations to predict the analytical spatial resolution of EPMA measurements.

DECREASING THE ACCELERATING VOLTAGE

Since the 1960s, it has been understood that to reduce the electron interaction in electron probe microanalysis volume—that is, to achieve greater spatial resolution—the accelerating voltage must be lowered (Anderson 1967).

Monte Carlo simulations (Fig. 3) demonstrate the critical importance of reducing the accelerating voltage from 15 kV down to less than half of that. Considering again an Fo_{80} olivine, the PENEPMA Monte Carlo simulations suggest that the electron interaction volumes for both tungsten and FE sources are significantly reduced. Using the 99% criterion, the tungsten Mg*K*α lateral width drops from ~2.2 μm to ~800 nm when going

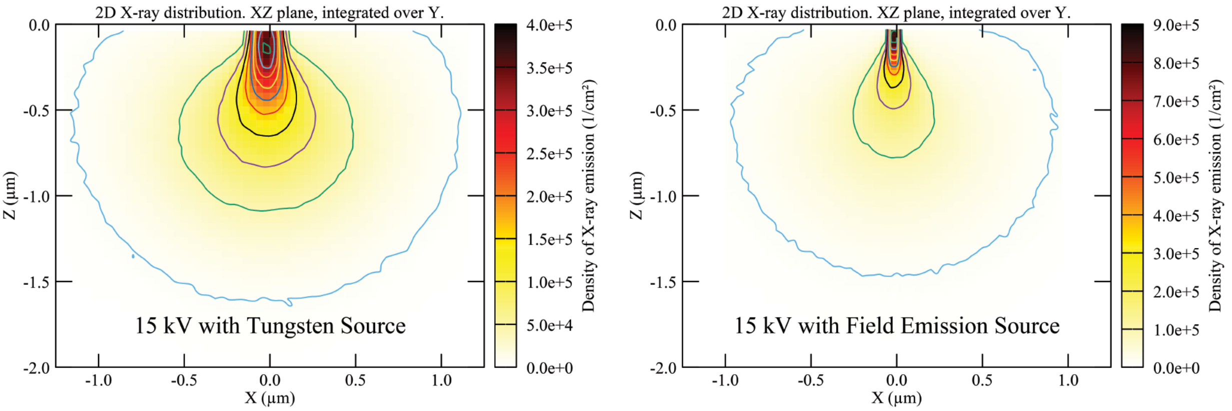

FIGURE 2. PENEPMA simulated vertical cross sections for Mg*K*α X-rays generated at depth in Fo_{80} olivine, with both 15 kV W-filament (210 nm diameter, **left**) and FE beam (35 nm diameter, **right**). Beam diameter values for 20 nA beam currents use estimates given in McSwiggen (2014) and Pinard and Richter (2016). Outer contour shows the bounding perimeter where generation of Mg*K*α X-rays drops to 1% of the maximum generated intensity; internal contours are for 10%, 20%, 30%, etc. Mg*K*α X-ray generation. Matrix absorption effect on the generated Mg*K*α X-rays is not included.

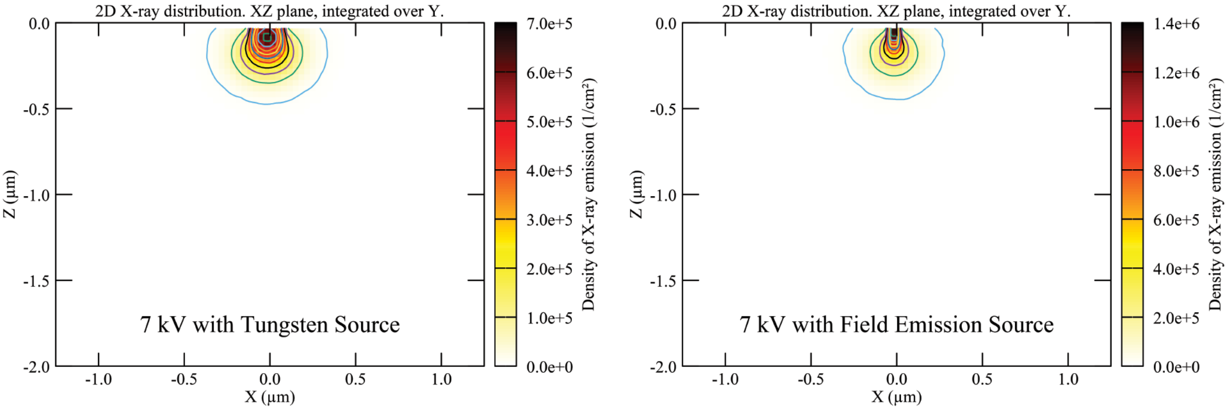

FIGURE 3. PENEPMA simulated vertical cross sections for Mg*K*α X-rays generated at depth in Fo_{80} olivine, with both 7 kV W-filament (210 nm diameter, **left**) and FE beam (35 nm diameter, **right**). Both FE and tungsten sources show much reduced zones of Mg*K*α X-ray generation with depth compared to the 15 kV simulations (Fig. 2). Note: these are models of X-ray generation and do not take into account matrix absorption.

from 15 to 7 kV. The maximum depth decreases from ~1.6 μm to ~500 nm and there is a similar reduction for FE lateral width, from ~1.75 μm to ~600 nm; and depth from ~1.5 μm to ~400 nm.

It is worth noting that at very low accelerating voltage or at very low overvoltage (depending on the X-ray line studied) and depending on the density and composition of the material analyzed, the diameter of the X-ray generation volume may approach the diameter of the electron beam. In such a case, the beam diameter, and thus the electron source type, will have a major influence on the size of the X-ray lateral spatial resolution.

These simulations show that the key factor for improved analytical spatial resolution is the accelerating voltage rather than the electron beam size. However, we note several things here: (1) FE imaging in the electron probe can provide the researcher with a more critical view for "targeting" the material to be probed, illuminating inclusions too small to be analyzed, but useful to *avoid* when focusing upon the host material, such as microlites in volcanic glass (K. Severn, pers. comm.) (2) The previous Monte Carlo simulations assume a uniform distribution of the electron beam density. It is possible that the FE source may have a denser electron density in the central core compared to the traditional Gaussian-shape of the tungsten and LaB_6 filaments, so that it may feasibly be possible to qualitatively image (X-ray map) at a tighter spatial resolution, while not enough for full quantitation. (3) The FE high electron density impacting the specimen can produce more damage than that from the tungsten filament, and in many cases operators of FE instruments (especially for geological materials) end up defocusing the beam—resulting in no gain in analytical spatial resolution compared with tungsten filament instruments. On the other hand, the FE's beam diameter remains smaller than from the comparable W source at high beam currents, and does not dramatically increase at low-kV, giving the operator a choice of smaller achievable beam diameters relative to W instruments. (4) There are anecdotal accounts of FE sources lasting for 5–10 years, so that the higher cost of the tip is more than offset relative to frequent replacements of tungsten tips, with long uninterrupted service. Thus, pros and cons must be weighed when making a purchasing decision for a new instrument.

Another factor affecting spatial resolution in EPMA is secondary fluorescence: X-rays generated, not by the incident high energy electrons, but by both characteristic and continuum X-rays. These secondary fluoresced X-rays can be generated from tens to hundreds of micrometers away, though are primarily a problem for trace element analysis in normal 15 to 20 kV EPMA. But for small, micrometer and sub-micrometer features, the "other" phase is very close and must be considered. Operation at low-kV reduces this effect somewhat as the high-energy characteristic X-rays (and the high-energy bremsstrahlung photons), the major source of production of secondary fluorescence X-rays, are no longer created. However, lowering the accelerating voltage does not completely eliminate this effect. Monte Carlo programs such as PENEPMA/PENELOPE have the ability to model the extent of secondary fluorescence and also provide the ability to correct for it (Llovet and Galan 2003).

PROBLEMS OF LOW-KV EPMA

It is clear that lowering the kV is important to achieve increased spatial resolution in EPMA (regardless of electron source). However, there are two main issues which became important when considering operating at low-kV: (1) X-ray lines generated and used at higher kV may no longer be available at lower kV, for example, the important element iron [the critical excitation energy for Fe*K*α is 7.114 keV (Zschornack 2007)]; and (2) because the electrons no longer penetrate deeply into the material, the state of the sample surface becomes more critical: the smoothness of surface polish, the surface fidelity and cleanliness, and the conductive coating (of both the unknown and the standard). And because the beam no longer penetrates nor spreads out radially as much, there is much more concentrated energy in a smaller region, and sample damage can be magnified significantly. These issues are discussed in several recent publications, e.g., Kearns et al. 2014; Saunders et al. 2014; Buse and Kearns 2015. However, we focus here upon the first issue, the problem of the L lines of a critical transition metal, iron, in a common rock-forming mineral, olivine.

Olivine was studied for two reasons: one, it is a relatively simple mineral phase, consisting dominantly of iron, magnesium, silicon, and oxygen but showing a wide compositional range. Second, olivine is a key constituent in the Earth's mantle and crustal rocks as well as extraterrestrial materials. EPMA analysis of small olivine grains or with complex zoning such as found in chondrules (Libourel and Portail 2018) or in diffusion and grain growth studies (Shea et al. 2015) might necessitate working at low-kV to achieve the desired spatial resolution.

THE PROBLEM OF LOW-KV EPMA OF FE-BEARING MATERIALS

It has been shown that it is difficult to do accurate EPMA with the *L*α lines of the transition metals using the traditional matrix corrections (ZAF, ϕ-rho-Z), e.g., Llovet et al. (2012), Gopon et al. (2013), and Buse and Kearns (2018). The reasons include peak shape changes and position shifts due to differences in bonding between the standard and the unknowns, as well as problems with the accuracy of mass absorption coefficients (MACs), with the *L*α peak lying directly across the absorption edge. There is a major increase in the MAC for Fe*L*α by Fe from right before the edge at 710 eV (Zschornack 2007), with a value of ~2180 cm^2/g at 704 eV (Heinrich 1987) to past the edge, with a value of ~14 400 cm^2/g at 717 eV (Heinrich 1987). This complex situation causes varying "self absorption" yields, and thus different MACs, for the same element for different Fe-bearing compounds—which is not the case for the MAC of the Fe*K*α X-ray line by atoms of Fe.

Gopon et al. (2013) found that the "non-traditional" *L*ℓ ("el el", L3-M1 transition) for Fe could be successfully utilized for quantification as it lay far from any Fe absorption edge. The use of the *L*ℓ line of Fe compared to the *L*α line works well for iron silicides, but its lower relative count rates in many minerals and glasses of interest to geoscientists leads to diminished statistical precision. To compensate for the low X-ray intensity of the Fe*L*ℓ line, measurements require longer counting times or the use of a monochromator crystal with a high detection efficiency. In addition, the Fe*L*ℓ line partially interferes with the Fe Ln line and the second order of diffraction of the Mg*K*α X-ray line. Therefore, the accuracy of quantification using the Fe*L*ℓ line in olivines at low to moderate Fe concentrations is increasingly dependent on the magnitude of the interference correction for Mg. Also, even though the *L*ℓ line originates from a transition between "inner" electron shells, recent studies by Terauchi and Sato (2018) show that the Fe*L*ℓ line peak position can shift between different iron oxides and then, potentially, between other iron compounds. Thus, it would be desirable if the analytical problems of the *L*α line could be resolved as to enable its use in low-kV EPMA. Llovet et al. (2016) found that for the transition metal Ni, if an empirical correction was applied to the fluorescence yield (a fundamental parameter in the matrix correction) of the Ni*L*α X-ray line, in addition to the reevaluation of the Ni*L*α MAC by atoms of Ni, there was an improvement in the matrix-corrected results. Following this methodology, Buse and Kearns (2018) recently evaluated the use of the Fe*L*α X-ray line for quantification of Fe in olivines in the compositional range between Fo_{91} and Fo_0. They showed that it was possible to achieve very good results with relative deviations to the expected Fe concentrations varying from 1 to 5%, at least for the olivines with FeO content ≥16 wt% (Buse and Kearns did not report quantification results using their method for olivines with lower FeO content). Their proposed method is to reevaluate the MACs of the Fe*L*α X-ray line by Fe in olivines at a given X-ray energy (or spectrometer position) as well as to evaluate partial fluorescence enhancement factors. Both factors vary smoothly with respect to the Fe concentration and can be interpolated using a regression fit. Thus, these coefficients can be used in ZAF or ϕ-rho-z matrix correction algorithms to quantify Fe using traditional k-ratios. The reference material (i.e., standard) they utilized for this approach was an Fo_{33} olivine from Dabbahu Volcano (Ethiopia), provided by a researcher at their institution. However, because of the proximity of the FeL_2 and L_3 absorption edges which lead to a rapid increase of the MAC with increasing X-ray energy, determining these coefficients using the described method can lead to close but different values of the MAC measured by different instruments/spectrometers due to differences in the resolution of the spectrometers used. To apply their proposed method, one will have to re-determine the MACs on their own instrument/spectrometers and a set of olivines reference materials. In addition, matrix correction algorithms allowing the use of different MAC values for the unknown and for the standard, in addition to the use of user-defined partial fluorescence yields, are not broadly available yet, making it difficult to utilize this method for routine applications.

MATERIALS AND METHODS

Electron probe measurements

The spectra of the Fe$L\alpha$-$L\beta$ X-ray lines were measured at the Eugene Cameron electron microscopy laboratory, Department of Geoscience, University of Wisconsin-Madison, using a CAMECA SXFiveFE electron microprobe, and at the Department of Earth Sciences, University of Minnesota using a JEOL JXA-8530FPlus electron microprobe. Both instruments used Probe for EPMA to collect the data (Donovan et al. 2018).

The JEOL JXA-8530FPlus is outfitted with the new Soft X-ray Spectrometer "SXES" that consists of an extended range diffraction grating JS2000, and a Peltier-cooled CCD camera (Terauchi et al. 2011). This type of spectrometer acquires the whole spectrum between 240 and 2800 eV simultaneously (similar to a SiLi or SDD EDS but with high spectral resolution).

Three wavelength-dispersive spectrometers (WDS) were used to record the spectra on the SXFiveFE microprobe and two WDS and the SXES were used on the JXA-8530FPlus microprobe (further details including monochromators used are given in Supplemental Materials[2], Table 1). All the spectrometers have a takeoff angle of 40°.

On the CAMECA instrument, 4 spectra covering the Fe$L\alpha$-$L\beta$ spectral range were acquired on each sample and then averaged together. The spectra were measured at 7 kV and 90 nA, from 0.686 to 0.734 keV with 500 steps and a dwell time of 1.8 s/step for the TAP crystals and 1.5 s/step for the PC0 pseudocrystal.

On the JEOL instrument, three spectra were accumulated for each sample with the WDS's and only one spectrum was recorded with the SXES, as this last detector is much more counting-efficient than the WDS. With the WDS, the spectra were recorded from 0.688 to 0.732 keV with 500 steps and a dwell time of 2.4 s/step. With the SXES, the spectra were recorded at 7 kV and 20 nA, from 0.236 to 2.830 keV with 4096 steps and a total counting time of 15 min. A 5 μm beam diameter was used for all the measurements on both electron microprobes.

The integrated areas of the spectra were calculated by numerical analysis using the trapezoidal rule. For the spectra recorded with the SXES detector, the step size is relatively large compared to the width of the X-ray lines. This implies a small underestimation of the calculated area using this spectrometer. The small error resulting from this underestimation will be partially cancelled out, and thus minimized, during the calculation of the area k-ratio as the Fe$L\alpha$-$L\beta$ X-ray line shapes of the olivine samples and of the Fe standard are very similar. Before the determination of the area integral, the background was fitted and removed using a linear curve for the TAP crystals and the SXES and using an exponential background for the PC0 crystal.

One concern that arises when measuring Fe in Fe-bearing materials using an electron beam is the change of the oxidation state of Fe due to interactions with the incident electrons. The change of Fe oxidation state under beam irradiation can lead to inaccuracies when measuring the X-ray intensity at the peak maximum or can lead to distortion of the recorded spectrum and it has been shown that the Fe peak position will shift toward the high energies when the oxidation state changes from Fe^{2+} to Fe^{3+} (Fialin et al. 2011). In olivine, which contains almost exclusively divalent Fe, such a change in the oxidation state is unlikely to occur but must be investigated nevertheless. A recent paper by Li et al. (2019) reports a method to observe the change in Fe oxidation by monitoring the variations of the X-ray intensity ratio Fe$L\beta$/Fe$L\alpha$ over time. We have monitored the Fe$L\alpha$ and Fe$L\beta$ X-ray intensities at 15 kV, 90 nA for 260 s with measurements at 10 s intervals on synthetic fayalite, Wards fayalite, and San Carlos olivine. The measurements were repeated at least three times on different locations and then averaged. No obvious change in the Fe$L\beta$/Fe$L\alpha$ ratio was observed (see Supplemental Materials[2], Fig. 1). This indicates that the Fe oxidation state in olivine is not altered by the electron beam.

Olivines

A set of nine olivine samples was used in this study. The intermediate Fe range ($Fo_{47–73}$) is covered by five olivines from (Aleutian) Shishaldin Volcano basalts (Fournelle 1988) and two olivines from the Smithsonian National Museum of Natural History: the Springwater olivine is from the microbeam standards collection (USNM 2566, Jarosewich et al. 1980) and the San Carlos is a "coarse" fraction from the same split as the USNM 111312/444 in the microbeam standards collection (T. Rose, E-mail communication, November, 16, 2012). The synthetic fayalite source (Finch et al. 1980) was Jill Banfield. The Wards fayalite is a sample from Crystal Park, Colorado (Barker et al. 1975).

These olivines' iron elemental concentrations range from 7.64 to 53.9 wt%. The olivine samples were characterized by EPMA at 15 kV and 20 nA, using the traditional $K\alpha$ X-ray lines, the PAP matrix correction algorithm (Pouchou and Pichoir 1991), and the MAC30 mass absorption coefficients (Heinrich 1987). At least 15 points were acquired to reduce the statistical uncertainties. The instrument used to measure the composition was a CAMECA SX51 microprobe at the Eugene Cameron electron microscopy laboratory, Department of Geoscience, University of Wisconsin-Madison, equipped with five WDS. The details of the oxide composition of each sample are given in Table 1 (and the corresponding stoichiometric formula are given in Supplemental Materials[2], Table 2). As further results of this paper are given in elemental wt%, those concentrations of Fe are also shown in Table 1. Particular attention was paid to select one homogeneous crystal (determined by BSE imaging and multiple EDS measurements) from each sample, and to focus on the same area for both the 15 and the 7 kV measurements.

TABLE 2. Re-quantification of the first set of olivine samples with the area k-ratio calibration curve using different positions and different grains

Sample name		Fe concentration (wt%)		
	Nominal	Sp1 (TAP)	Sp2 (TAP)	SP4 (PC0)
Coarse San Carlos Mnt 61	7.75(12)	7.46	7.38	7.17
SH15 small Fo88.3 Mnt 62	9.57(41)	7.99	7.71	8.30
USNM Springwater 2	13.20(7)	12.95	13.02	13.19
USNM Springwater 1	13.22(19)	12.72	13.21	13.16
SH15 Big Fo72.7 Mnt 62	19.01(12)	17.08	15.7	18.28
SH11 #7 core Fo72	19.79(25)	19.67	18.7	20.14
SH9 Fo67.6 Mnt 62	21.35(16)	21.46	20.58	21.43
SH11 small Fo64	23.65(17)	23.86	23.70	24.12
SH9 Fo62.6 Mnt 62	24.66(13)	24.19	23.83	24.46
SH11 #11 small Fo52	30.21(18)	30.31	29.21	29.36
Wards Fayalite Mnt 61	50.79(23)	48.26	48.21	51.48
Rockport Fayalite Mnt 30	52.27(23)	48.33	47.79	50.23
Synthetic Fayalite Mnt 61	54.55(33)	52.03	53.48	55.00
Fe metal 1	100.0	99.98	99.99	100.00
Fe metal 2	100.0	100.00	100.00	99.99

Notes: The measurements where performed at 7 kV and 90 nA with the SX51 microprobe using three different WDSs. Numbers in parentheses are the estimated standard deviations (uncertainties on the last digits).

TABLE 1. Oxide composition (wt%) of olivines, measured at 15 kV using the traditional $K\alpha$ lines with the CAMECA SX51 instrument

	SiO_2 (wt%)	FeO (wt%)	MnO (wt%)	MgO (wt%)	CaO (wt%)	Total (wt%)	Fe (wt%)
Synthetic fayalite	28.79(13)	69.35(48)	0.20(4)	0.02(1)	0.00(2)	98.36(50)	53.90(31)
Wards fayalite	29.31(19)	64.89(60)	4.49(38)	0.50(7)	0.09(4)	99.29(74)	50.44(30)
SH111	34.44(15)	41.93(43)	0.86(5)	21.10(11)	0.22(1)	98.55(47)	32.59(24)
SH11	34.96(25)	38.80(55)	0.86(5)	24.26(22)	0.26(2)	99.15(64)	30.16(24)
SH25	36.34(24)	33.89(98)	0.69(6)	28.66(73)	0.25(3)	99.83(1.25)	26.34(22)
SH9	37.49(20)	27.33(35)	0.57(5)	34.21(28)	0.18(1)	99.78(49)	21.25(20)
SH15	38.77(28)	23.98(39)	0.38(3)	38.09(30)	0.19(2)	101.41(56)	18.64(19)
USNM Springwater	39.82(20)	16.90(2)	0.32(11)	43.64(2)	0.02(17)	100.70(29)	13.14(16)
USNM San Carlos	40.95(25)	9.62(23)	0.14(4)	48.93(28)	0.10(2)	100.10(44)	7.64(12)

Notes: The elemental Fe concentration is also given in the last column. Numbers in parentheses are the estimated standard deviations (uncertainties on the last digits).

Carbon contamination

To study and mitigate the effects of carbon contamination during spectra acquisition, a custom cryo-chiller replacing the liquid nitrogen dewar used to cool the CAMECA cold plate was used to perform the measurements on the CAMECA SXFiveFE instrument. This anticontamination device was able to decrease the temperature in the microprobe chamber to about –150 °C and reduced the vacuum to as low as 8×10^{-7} Pa. In addition to freezing the volatile contaminants, the cryo-chiller also cooled the samples by radiative transfer, reducing the mobility of contaminants on the sample surface.

To study the effects of carbon contamination on the measurements, long spectrum acquisitions (~19 min for each spectrum) were performed first by recording the spectrum from low X-ray energies to high X-ray energies and then by repeating the measurements from high to low X-ray energies on a new spot. Any significant amount of carbon contamination deposited during spectrum acquisition should distort the spectrum by decreasing the electron landing energy and increasing the absorption of the emitted X-rays. These effects, more pronounced at the end of the acquisition than at the beginning, should result in different appearances between the two spectra.

Spectrum acquisitions were performed on pure Fe, USNM Spring Water olivine, San Carlos olivine, Wards fayalite, and synthetic fayalite, covering the entire range of Fe concentrations. The measurements were performed at 7 kV and 90 nA using three WDS (LTAP, TAP, and PC0 monochromator crystals as described in Supplementary Materials[2], Table 1). X-rays were recorded with 100 steps and for photon energies ranging from 685.8 to 733.7 eV for the LTAP crystal, from 684.8 to 732.7 eV for the TAP crystal, and from 582.5 to 892.3 eV for the PC0 crystal. Three different spectra were measured on each sample and each direction and averaged together (the averaged spectra are shown in Supplementary Materials[2], Fig. 2).

The spectra measured in both directions show no significant differences in peak shape or intensities on either the background or the tails of the peaks. The only noticeable differences are slightly less intense peak maxima for the $L\alpha$ line and more intense maxima for the $L\beta$ line when the spectrum was recorded from high to low energies relative to the other direction. This difference is well explained by an increase of the carbon contamination thickness during acquisition. However, the differences between the spectra are typically within the uncertainties of the counting statistics associated with the measurements. The maximum relative standard deviation (RSD) of the calculated areas of the Fe$L\alpha$-$L\beta$ X-ray lines between spectra measured in opposite directions was found to be 1.8% for the Spring Water olivine (low Fe concentration) when measured with the TAP crystal (low detection efficiency, large statistical fluctuations). Nevertheless, all data used to derive the calibration curves came from the spectra measured with increasing spectrometer positions, i.e., with decreasing photon energy (except for the SXES where this is not relevant) to be consistent.

The changes in peak area due to carbon contamination remain generally very small, with mean RSD found to be 0.8, 1.3, and 0.4% for the LTAP, TAP, and PC0 monochromator crystals, respectively. This indicates carbon contamination has no significant effect on the measurements when using a cryo-chiller at these experimental conditions. No cold trap or other anti-contamination devices were used in the JEOL JXA-8530FPlus instrument or, later, in the CAMECA SX51 instrument. However, the obtained results (the area k-ratios) agree within the uncertainties with the results obtained on the CAMECA SXFiveFE instrument using the cryo-chiller. This indicates that even when no anticontamination devices are used, carbon contamination effects are not significant enough to significantly affect the measurements.

RESULTS

We studied utilization of the Fe$L\alpha$ line for low-kV EPMA in a set of olivines as well as a set of iron silicides (Moy et al. 2019). An essential part of this involved attempting to determine the Fe$L\alpha$ MACs, which lead to a reevaluation of the procedures used to measure them. This reevaluation, going back to fundamental parameters, sheds light on why it is so difficult to determine the correct MAC in the energy/wavelength region at the Fe$L\alpha$ peak position, which lies across the Fe L_3-edge position.

All measured X-ray peaks are broader than they would appear naturally: their shapes are considered to be Voigt profiles, convolutions of two broadening mechanisms, one being the Lorentzian profile for the natural width of the peak, the other the Gaussian profile for the broadening by the specific spectrometer being used (Rémond et al. 1993). However, direct determination of the MAC of the Fe$L\alpha$ peak from an iron silicide or olivine was found to be impossible. Any attempt to measure precisely the MAC at any single peak channel is not possible because of the Gaussian broadening of the spectrometer and the rapidly changing MAC value under the energy range of this Gaussian. Ultimately, if it were possible to correctly measure the MACs for a range of iron-bearing phases, they would define a three-dimensional plot, as functions of both specific energy/wavelength as well as Fe content. A full explanation and theoretical derivation proving the futility of determining MACs for Fe-bearing phases, using the traditional EPMA approach (e.g., XMAC (Pouchou 1996)) is given in Moy et al. (2019).

Traditional quantification method with the Fe*Lα* X-ray line

To corroborate the need for an improved quantification method when using the Fe$L\alpha$ X-ray line at 7 kV, we tried to quantify our set of olivines, previously characterized at 15 kV using the Fe$K\alpha$ X-ray line, by varying the primary standards: (1) the pure Fe standard as it was used to perform the quantification using the $K\alpha$ X-ray line, (2) the Wards fayalite standard as representative of commonly used Fe standards in EPMA for geological work, and (3) the SH111 standard as the one with the highest Fe abundance and a substantial amount of Mg in our set of olivines. The quantification results, performed using the PAP matrix correction algorithm (Pouchou and Pichoir 1991) and the MAC30 MAC data table (Heinrich 1987), are very poor (see Supplementary Materials[2], Table 3) and yield RSD of up to 60% compared to their nominal Fe concentration, as seen in Figure 4. The only adequate results are obtained when the Fe quantification of an olivine is performed using itself as a primary standard. These poor quantification results can be attributed to changes of the atomic parameters (MAC and fluorescence yield) between the different olivine and pure Fe samples. These parameters, in addition to not being known precisely except for pure Fe, will differ between the quantified olivine and the standard, and traditional matrix correction algorithms do not support different atomic values for the unknown and the standard. It is also worth noting that the RSD increases with increasing Fe content in the olivines at approximately the same rate, regardless of the standard used. These results show that quantification of Fe in olivines with the $L\alpha$ X-ray line cannot be done using the traditional quantification method.

TABLE 3. Quantification of a second set of olivines at 7 kV and 90 nA using the area k-ratio calibration curve with the SXFiveFE microprobe and three WDS

Sample name	Fe concentration (wt%)			
	Nominal	Sp1 (LTAP)	Sp2 (TAP)	SP4 (PC0)
WKOL no. 1	4.11(14)	3.92	4.34	3.54
HaKOL g3 no. 8	5.98(6)	6.22	6.32	5.44
UWOL-1 no. 4	7.94(4)	8.01	8.64	7.19
SWOL-1 no. 2	13.22(8)	13.05	13.71	12.63
SWOL-1 no. 2 ROM	13.22(8)	13.67	14.00	12.97
KNOL-2 no. 6	15.44(11)	15.41	15.60	14.04
FJOL no. 5	18.76(8)	18.68	18.62	18.04
OROL no. 20	26.78(4)	26.88	26.77	25.93
Rockport Fayalite Mnt 30 Rand	52.50(23)	51.74	50.48	52.29
Synthetic Fayalite Mnt 61 (new pos)	54.80(33)	53.44	52.98	52.24
Fe metal	100.0	99.99	99.99	99.99

Notes: Nominal refers to the 15 kV measurements using the traditional Fe$K\alpha$ X-ray line. Numbers in parentheses are the estimated standard deviations (uncertainties on the last digits).

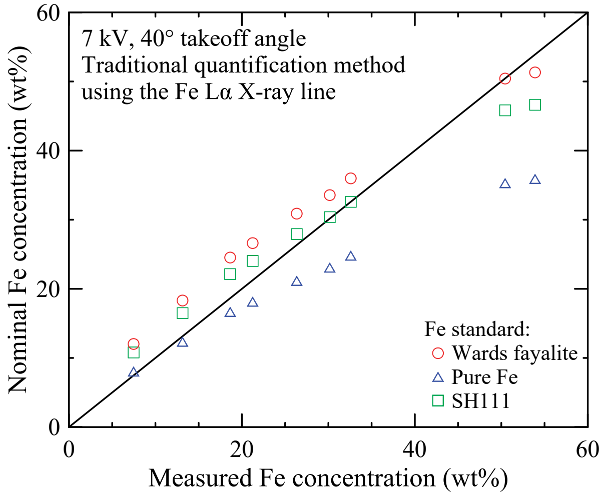

FIGURE 4. Quantification of the first set of olivine samples using the traditional quantification method and the Fe*L*α X-ray line at 7 kV. Three Fe standards were used to perform the quantification. Regardless of the standard used, large deviations from the nominal Fe concentration are observed.

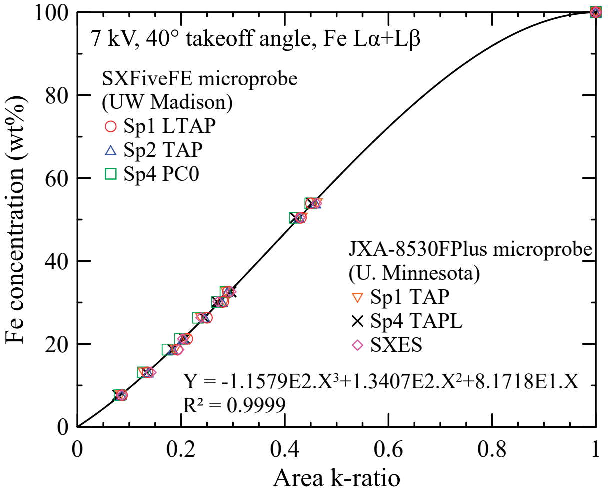

FIGURE 5. Integrated Fe*L*α+*L*β k-ratios acquired at 7 kV on two different instruments with six different spectrometers. The olivine peak area measurements were normalized to the peak area value obtained on the pure Fe standard.

Plot of Fe*L*α+*L*β k-ratio vs. Fe content

After much time and effort evaluating the Fe*L*α-*L*β spectra of both iron silicides and olivines, and realizing that there were insurmountable obstacles to determining the Fe*L*α MACs correctly, another approach was called for. What to do? When in doubt, make a plot. And so, combined-integrated k-ratios were determined: we integrated the areas under the Fe*L*α-*L*β wavescan peaks and subtracted the backgrounds, for both the experimental samples and a pure iron standard, and then created "area k-ratios" using the pure iron standard. When these integrated Fe*L*α-*L*β wavescan area k-ratios were plotted against the sample Fe-content (Fig. 5), a simple relationship became obvious (experimental k-ratios are given in Supplemental Materials[2], Table 4).

There is a strong degree of direct correlation between the integrated Fe*L*α+*L*β k-ratios and the Fe content of the olivines. The data can be fitted by a simple third-order polynomial (with conditions of being 0 when the area k-ratio is 0 and being as close as possible to 100 when the area k-ratio is 1) with an R^2 value of 0.999.

This simple approach allows the X-ray intensity of the integrated Fe*L*α-*L*β peak to be used to quantify the iron content of olivines. We suggest it can be applied to *any* conventional electron microprobe; the only limitation is having a spectrometer takeoff angle of 40°, the accelerating voltage being 7 kV and the standard to calculate the k-ratio being pure Fe. It entails (1) the measurement of the area of Fe*L*α-*L*β spectrum of the olivines being studied, (2) the same measurement on a pure Fe metal standard (a common, easily available standard), and removing the backgrounds for both the olivine and the Fe metal standard, and (3) using the following calibration curve (Eq. 1) to read out the Fe wt% of the olivine:

$$\text{Fe wt\%} = 81.718 \times K + 134.07 \times K^2 - 115.79 \times K^3 \qquad (1)$$

where K is the area Fe*L*α+*L*β k-ratio. This elemental Fe value would then be input into the matrix correction software as a defined element, with the other elements quantified using the traditional matrix correction.

TABLE 4. Re-quantification of the Fe concentration of the two sets of olivines using the calibration curves obtained using the Fe*L*α peak maximum

		Fe concentration (wt%)		
		SXFiveFE		
Sample name	Nominal	Sp1 (LTAP)	Sp2 (TAP)	Sp4 (PC0)
First olivine set				
USNM San Carlos	7.64(12)	7.38	7.73	7.23
USNM Springwater	13.14(16)	12.75	12.63	12.57
SH15	18.64(19)	19.56	18.55	18.88
SH9	21.25(20)	22.24	21.98	21.53
SH25	26.34(22)	28.01	28.51	26.45
SH11	30.16(24)	31.75	31.08	30.89
SH111	32.59(24)	35.06	33.25	33.07
Wards fayalite	50.44(30)	50.74	51.39	49.99
Synthetic fayalite	53.90(31)	52.43	52.19	53.03
Fe metal	100.0	99.60	99.60	99.55
Second olivine set				
WKOL no. 1	4.11(14)	3.98	3.85	4.16
HaKOL g3 no. 8	5.98(6)	5.86	5.98	6.37
UWOL-1 no. 4	7.94(4)	7.52	7.41	8.22
SWOL-1 no. 2	13.22(8)	13.05	13.43	13.98
KNOL-no. 6	15.44(11)	13.41	14.19	14.66
FJOL no. 5	18.76(8)	17.95	18.50	18.95
OROL no. 20	26.78(4)	26.49	27.30	27.59
Rockport fayalite Mnt 30 Rand	52.50(23)	51.74	51.41	52.03
Synthetic fayalite Mnt 61 (new pos)	54.80(33)	52.81	53.18	53.55
Fe metal	100.0	99.60	99.60	99.55

Notes: The results were obtained at 7 kV and 90 nA with the SXFiveFE microprobe and three WDS. Numbers in parentheses are the estimated standard deviations (uncertainties on the last digits).

DISCUSSION

Theoretical derivation of area k-ratio

Why would this apparently simple calibration curve work, and we assert, work on any electron microprobe? To understand this, we enter the realm of the physics used to go from the raw X-ray intensities, via the so-called "matrix correction," to the final corrected element values. Most people delve as far as the so-called ZAF correction, which was a highly simplified expression needed when computing power was minimal. But it all rests upon a strong physical basis, the so-called fundamental equation of the microanalysis, which can be written as:

$$I_X\left(E_{\mathrm{ph}}\right)=C_A\frac{N_a}{A_r}n_{\mathrm{el}}\omega_{\mathrm{i}}^{\mathrm{A}}\Gamma_{\mathrm{ij}}^{\mathrm{A}}Q_{\mathrm{i}}^{\mathrm{A}}\left(E_0\right)\int_0^\infty\varphi_i\left(\rho z\right)e^{-\frac{\mu}{\rho}\left(E_{\mathrm{ph}}\right)\frac{\rho z}{\sin\theta_{\mathrm{d}}}} d\rho z\left[\varepsilon\frac{\Delta\Omega}{4\pi}\right]\left(E_{\mathrm{ph}}\right)F\left(1+g_{\mathrm{CK}}\right) \tag{2}$$

where $I_X(E_{ph})$ is the number of characteristic X-rays of energy E_{ph} recorded per unit of time for the X-ray line of interest, C_A is the concentration of the studied element A, N_a is the Avogadro number and A_r is the atomic weight of element A. n_{el} is the number of primary electrons reaching the sample per unit of time, ω_i^A is the fluorescence yield for the element A and a primary ionization in the shell i (i.e., the probability of emitting a photon during relaxation of atom A with an initial vacancy in the electronic shell i). Γ_{ij}^A is the transition rate from shell j to i (i.e., the probability that the relaxation occurs by the transition of an electron from the shell j to the vacancy located in shell i). $Q_i^A(E_0)$ is the ionization cross section (in cm^2) of the shell i of element A by impact of electrons with energy E_0. $\varphi_i(\rho z)$ is the so-called ϕ-rho-z function representing the depth distribution of ionization of electronic shell i of element A at mass depth ρz inside the sample for an incident electron beam of energy E_0. The next term in Equation 2, corresponding to the exponential factor, represents the attenuation of the created X-rays inside the sample before they reach the surface with an angle θ_d corresponding of the takeoff angle of the detector. $\mu/\rho(E_{ph})$ is the MAC (in cm^2/g) of the sample for a photon of energy E_{ph}. ε and $\Delta\Omega/4\pi$ are the intrinsic detection efficiency of the spectrometer for photons of energy E_{ph} and the geometric detection efficiency of the spectrometer also for photons of energy E_{ph}, respectively. F represents the secondary fluorescence enhancement factor ($F \geq 1$) and the $(1+g_{CK})$ factor represents the X-ray intensity enhancement by Coster-Kronig and super-Coster-Kronig effects. The X-ray intensity calculated by Equation 2 corresponds to the intensity of a single characteristic X-ray. In the case where several characteristic lines are considered, the total X-ray intensity becomes the sum of the X-ray intensities of each of the considered lines, each intensity is calculated using Equation 2 with the appropriate atomic parameters.

This equation works well in the general case, but it assumes some simplifications that can be problematic in certain circumstances. One drawback of this equation is the fact that the characteristic X-ray is supposed to be emitted at an exact energy E_x. In reality, the X-ray line has a natural width (also called natural broadening) following a Lorentzian shape for the inner shell transitions and with its maximum centered on E_x.

In addition, the spectrometer response function must also be taken into account. This function depends on the X-ray energy recorded (E_{ph}). In the case of crystal monochromators, because of crystal imperfections such as mosaic misorientation (Bertin 1975), the detector response function will not be a Dirac (δ) function following Bragg's law, i.e., not only the wavelength satisfying $n\lambda = 2d\sin(\theta)$ will be reflected. Instead, wavelengths of radiation length $\lambda + d\lambda$ will also be reflected but with a reduced intensity, which decreases rapidly as dλ increases. The detector response function can be well described by a Gaussian function centered on the recorded wavelength λ_X (or on the recorded energy E_x in an energy representation) and characterized by a full-width at half maximum Γ_G. When recording the X-rays at an energy E_{ph}, all the photons in a range $[E_{ph}–3\Gamma_G; E_{ph}+3\Gamma_G]$ are appreciably reflected by the crystal, with an intensity proportional to the Gaussian function. With traditional WDS, the X-rays are usually detected by a flow gas detector or by a sealed gas detector. The response function of this detector is usually represented by an integrator: all the photons reaching the detector are detected, without discrimination of their energy. An energy window can be used to discriminate high order X-ray reflections (corresponding to higher energies) but cannot distinguish photons in an energy range as small as $[E_{ph}–3\Gamma_G; E_{ph}+3\Gamma_G]$.

The natural spectrum, i.e., the spectrum emitted from the sample before detection, is described by the product of the emitted intensities I_x with the area-normalized Lorentzian functions. The recorded spectrum is then the convolution of the natural spectrum with the spectrometer response function. More details are given in Moy et al. (2019). When I_x is not dependent on the X-ray energy, i.e., when

$$\left[\varepsilon\frac{\Delta\Omega}{4\pi}\right]\left(E_{\mathrm{ph}}\right) \text{ and } \frac{\mu}{\rho}\left(E_{\mathrm{ph}}\right)$$

are constant over the X-ray energy range effectively recorded by the spectrometer due to its instrumental broadening (typically from $E_{ph}–3\Gamma_G$ to $E_{ph}+3\Gamma_G$), the X-ray intensity can be extracted from the previously mentioned convolution product. Consequently, by normalizing the unknown intensity with an intensity recorded on a standard sample, and assuming that the natural broadening of the X-ray line and the spectrometer broadening are the same for both the unknown and the standard, the remaining convolution product will be the same for the unknown and the standard and will cancel out during the calculation of the so-called k-ratio. One can then obtain the k-ratio traditionally used to perform quantitative EPMA.

However, in the case of the Fe*L*α and *L*β X-ray lines, the MAC changes rapidly over the spectrometer broadening energy range because of the nearby presence of the L_2 and L_3 absorption edges (and can additionally vary due to different compositions and bonding environments between the standard and the unknown), and so the X-ray intensity, I_x, cannot be extracted from the above-mentioned convolution—which is what is typically done in "normal EPMA." The broadening effects now do not cancel out and so the measured k-ratio still depends on the spectrometer broadening, i.e., of the instrument used, and hence will not be suitable for a universal ZAF or ϕ-rho-Z matrix correction.

Fortunately, by integrating the intensity of the X-ray lines of interest over the whole energy range—theoretically from –∞ to +∞, but in practice over the energy range of the Fe*L*α-*L*β spectrum where the characteristic X-ray intensity is not negligible—the integral of the convolution product can be separated into the product of two integrals:

$$\int_{-\infty}^{+\infty}\int_{-\infty}^{+\infty}I_X\left(E\right)L\left(E\right)G\left(E-E_{\mathrm{ph}}\right)\mathrm{d}E\mathrm{d}E_{\mathrm{ph}}=\int_{-\infty}^{+\infty}I_X\left(E\right)L\left(E\right)\mathrm{d}E\int_{-\infty}^{+\infty}G\left(E\right)\mathrm{d}E \tag{3}$$

where $L(E)$ and $G(E)$ represent the Lorentzian (the natural broadening) and Gaussian (specific detector broadening) contributions to the spectrum, respectively. Notice that when several X-ray lines are considered, *L*(*E*) is replaced by a sum of Lorentzian functions corresponding to the different transitions, such as the Fe$L\alpha_1$, Fe$L\alpha_2$, and Fe$L\beta_1$ X-ray lines, at the condition that $I_X(E)$ is also replaced by a sum of X-ray intensities, each corresponding to the different transitions taken into account and each being calculated by means of Equation 2 using the appropriate atomic parameters. Other transitions, far from those of interest, can be disregarded as we only calculate the area for the Fe*L*α-*L*β X-ray lines and they are not interfering with these lines of interest.

By calculating the k-ratios using the area of the X-ray lines (noted kr_{Area}), where the superscript *u* is for the unknown and *s* is for the standard, we obtain:

$$kr_{Area} = \frac{\int_{-\infty}^{+\infty} I_X^u(E)L(E)dE \int_{-\infty}^{+\infty} G(E)dE}{\int_{-\infty}^{+\infty} I_X^s(E)L(E)dE \int_{-\infty}^{+\infty} G(E)dE} = \frac{\int_{-\infty}^{+\infty} I_X^u(E)L(E)dE}{\int_{-\infty}^{+\infty} I_X^s(E)L(E)dE} \quad (4)$$

The k-ratio in Equation 4 is now independent of the spectrometer broadening and hence suitable for the creation of a universal calibration curve. The only limitation that remains is that the takeoff angle of the detector (included in the term I_X) must be of 40°, as is the case for most of the commercially available electron microprobes today (in particular the JEOL and CAMECA instruments used in this study).

Calibration curve using the *L*α+*L*β area

The integrated areas of the Fe*L*α-*L*β spectra measured on each olivine sample were normalized to the area integral obtained on the pure Fe standard (area k-ratio) and plotted as a function of the Fe concentration, shown previously in Figure 5.

The experimental data follow a smooth increase with increasing Fe concentration. We found that values are very similar from one spectrometer to another, independent of the spectrometer used, and in agreement with the theoretical treatment. Therefore, data across instruments and spectrometers were averaged subsequently. The averaged data were fitted by a third-order polynomial under the physical conditions that the Fe concentration is equal to 0 when the area k-ratio value is 0 and equal to 1 when the area k-ratio value is 1. As shown in Figure 6, the resulting fit is very good with a regression factor of 0.999. While the data measured on the SH111 and Wards fayalite olivine samples have the highest RSD, the values still agree with the fitting curve within the statistical uncertainties.

Testing the calibration curve

The quantification of olivines based on this new approach follows a two-step process: first, the Fe concentration is determined with the area k-ratio calibration curve using Fe metal as a standard and then, fixing this Fe value in the matrix correction, the other elements are quantified using the traditional method with measured k-ratios.

The calibration curve was tested again on a subset of our olivine samples, but using different grains and using a different electron microprobe (CAMECA SX51 at the University of Wisconsin-Madison) and some additional olivines with good results. Each olivine grain was quantified again at 15 kV using the traditional Fe*K*α X-ray lines prior to spectra acquisition to account for any inter-grain compositional variability. Three WDS were tested: two TAP crystals (2d = 25.745 Å) and a PC0 crystal (2d = 45.0 Å). Comparisons of the nominal Fe concentrations measured at 15 kV with the Fe concentrations measured at 7 kV using the calibration curve are given in Table 2 and shown on Figure 7.

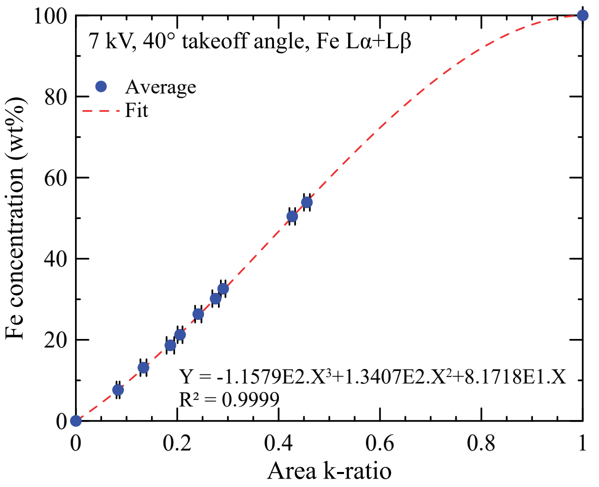

FIGURE 6. Calibration curve obtained by measuring the Fe*L*α and *L*β spectra at 7 kV on all olivine samples and averaging the results. The area k-ratio has been obtained relative to the pure Fe sample by integrating the Fe*L*α-*L*β spectrum (area method). (Error bars representing the standard deviation of the experimental data are also plotted).

Very good results are obtained with the PC0 crystal with almost all the samples with the exception of the Rockport fayalite where Fe was underestimated by 2.28 wt%. Both TAP crystals gave reasonably good results for almost all the samples but also highly underestimate the Fe concentration of the Rockport fayalite. This may indicate a problem with (1) the nominal composition of this sample (even if it has been re-acquired prior to the measurement, the spectra were acquired at close, but different positions and local heterogeneities on the fayalite (Rose et al. 2009) can explain the seen deviations), (2) a tilt of the sample or sample holder, changing the takeoff angle, or (3) a problem with the calibration curve itself. The latter seems unlikely to be the explanation as for the PC0 crystal, the Fe composition of the Rockport fayalite samples are well reproduced and the calibration curve varies smoothly everywhere. The spectrometer number 2 underestimated the Fe concentration in general, which can be attributed to its relatively low X-ray intensity yield (lower than for the two other spectrometers) making the recorded spectra noisier and therefore, making the background removal less accurate. An overestimation of the background leads to an underestimation of the peak area and then to an underestimation of the Fe concentration.

In addition, the calibration curve was also tested on a different set of olivines using the CAMECA SXFiveFE instrument, following the same experimental protocol and the obtained Fe concentration, in wt%, are given in Table 3 and plotted in Figure 8. The k-ratio vs. nominal Fe concentration curve acquired on these samples is in very good agreement with the previously acquired

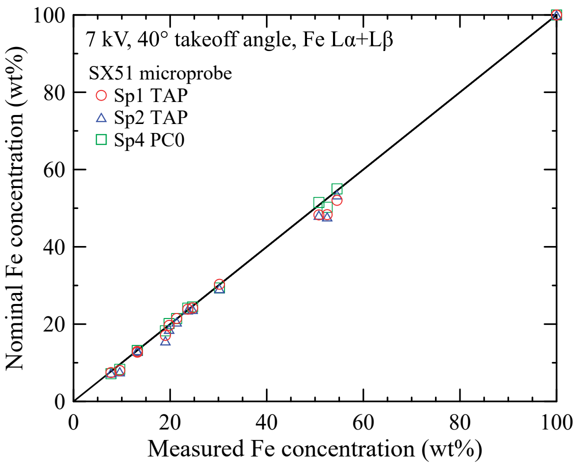

FIGURE 7. Quantification of the first set of olivine samples using the calibration curve (Eq. 1) determined at 7 kV. The measurements were performed on the SX51 instrument using three different WDS.

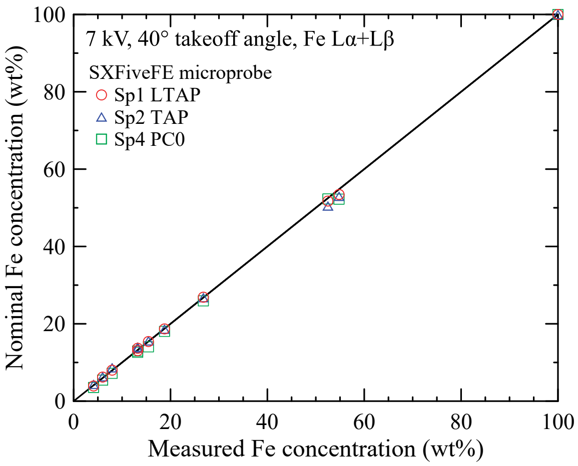

FIGURE 8. Quantification of a second set of olivine samples using the calibration curve (Eq. 1) at 7 kV. The measurements were performed on the SXFiveFE microprobe with three different WDS.

calibration curve. Hence, the Fe concentrations determined using the calibration curve (Eq. 1) are also in good agreement with the expected concentration, as shown in Table 3. Again, the determined Fe concentration for the fayalite samples is underestimated especially for the spectrometer number 2 which has the lowest detection efficiency. Except this deviation, other results are in very good agreement with the expected Fe concentrations, demonstrating the robustness of this analytical approach irrespective of instrument, spectrometer, and crystal choices. It is worth noting that the area calibration curve is also robust against the spectrometer energy drift (change of the maximum peak position over time) as the entire spectrum is recorded and integrated.

Calibration curve using the maximum intensity of the *L*α X-ray line

The drawback of the area intensity method is the long acquisition time for each spectrum. The combination of the calibration curve approach with traditional k-ratios was tested as a means to shorten acquisition times. Intensity measurements using the SXFiveFE and SX51 instruments were acquired on the olivine samples at the maximum intensity of the Fe*L*α X-ray line and on each side of the Fe*L*α-*L*β peaks (at 0.686 and 0.733 keV for the LTAP and TAP crystals and at 0.583 and 0.830 keV for the PC0 crystal) to subtract the background. The X-ray intensity was also measured on the pure Fe standard and a traditional k-ratio was calculated. When plotted against the Fe concentration, similarly to what has been obtained in the simpler case of the Fe*K*α line by Keil and Fredriksson (1964), the k-ratios follow a smooth curve that can easily be fitted by a third-order polynomial as seen on Figure 9. However, when the Fe concentration is plotted as a function of the experimental k-ratio, we were not able to obtain a satisfactory fit using established mathematical functions. The previously found third-order polynomial cannot be inverted and used for practical application as it has two complex roots. With the help of a spreadsheet program, the fitting polynomial can easily be evaluated and tabulated for a large number of Fe concentrations, ranging from 0 to 100 wt%, with a small given step (e.g., 0.5 Fe wt%). The unknown k-ratio and the corresponding Fe concentration can then be obtained by linear interpolation of the closest values found in the spreadsheet. The obtained third-order polynomials are varying slowly with the k-ratio, and thus a linear interpolation is a good approximation of the searched values, as long as the tabulation step is small enough.

In agreement with the theory discussed in section "Theoretical derivation of area k-ratio," these k-ratios are still dependent on the spectrometer efficiency. Hence, the obtained calibration curves are different for each spectrometer as shown on Figures 9a and 9b. However, the two spectrometers, Sp1 (LTAP or TAP crystal) and Sp2 (TAP crystal), give almost the same fitting curve as their instrumental broadening is very similar.

These "non-universal" calibration curves were obtained on the SXFiveFE and the SX51 instruments. On the SXFiveFE microprobe, the curves were deduced from measurements performed on the two sets of olivine previously described in this paper. Only the first set of olivines was used to derive the curve on the SX51 instrument. The measurements were performed at 7 kV and 90 nA. The obtained curves were then used to re-quantify the Fe concentration in the olivines. The results, shown in Tables 4 and 5, give satisfactory quantitation numbers. The highest average absolute deviation is seen for the synthetic fayalite samples where the predictions underestimate the nominal values up to 2.42 wt%. The determination of this peak maximum calibration curve, despite its "non-universal" character, is easier and less time consuming than the calibration curve obtained using the peak area. The only drawback is that it requires a calibration curve to be acquired for each spectrometer. The calibration curve gives good quantification results, especially when using the high-counting rate PC0 crystal even despite the overlap with both the Fe*L*β X-ray line and the L_3 absorption edge.

It is of historical interest that Castaing, the father of EPMA, proposed in his landmark 1952 thesis (English translation in 1955) a simple version of what we show here: an "α correction factor" for simple binary compounds, which was developed in more practical detail a decade later by Ziebold and Ogilvie (1963) and ultimately into the Bence and Albee (1968) correction factors for geological materials.

This method is more convenient to use than the area k-ratio

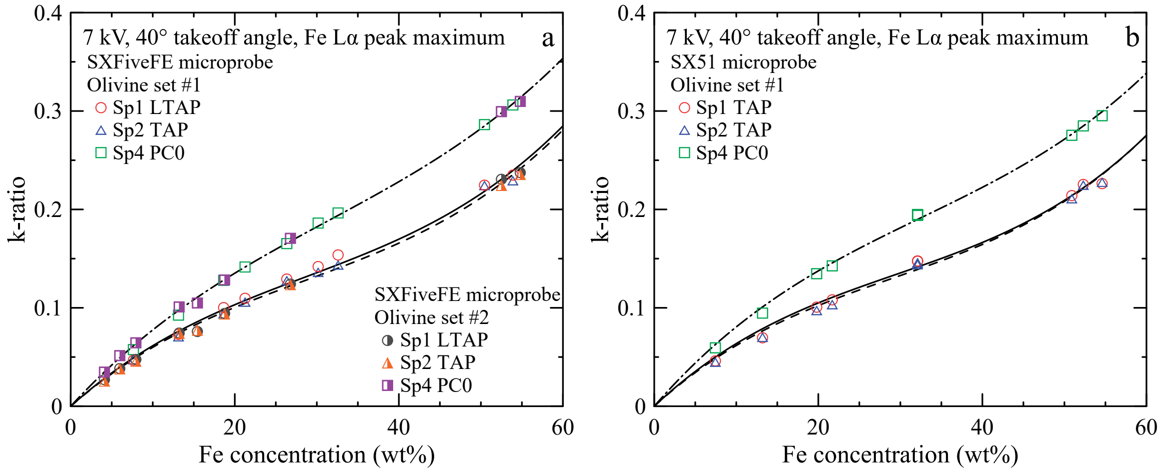

FIGURE 9. Calibration curves based on the maximum net peak intensity of the Fe*L*α X-ray line acquired with the SXFiveFE (**a**) and SX51 (**b**) microprobes. The curves obtained for the LTAP (continuous line) and TAP (dashed line) crystals are very similar.

TABLE 5. Reevaluation of the Fe concentration of the first set of olivines using the calibration curves obtained using the Fe*L*α peak maximum

Sample name		Fe concentration (wt%)		
		SX51		
First olivine set	Nominal	Sp1 (TAP)	Sp2 (TAP)	Sp4 (PC0)
Coarse San Carlos	7.46(77)	6.94	6.98	7.13
USNM Springwater	13.20(7)	11.52	12.08	12.43
SH11 Fo72	19.79(25)	19.26	19.02	19.80
SH9 Fo67	21.70(30)	21.43	20.77	21.46
SH111 Fo47 no. 1	32.12(22)	33.69	33.90	33.30
SH111 Fo47 no. 2	32.12(22)	33.76	33.39	33.08
SH111 Fo47 no. 3	32.12(22)	33.69	33.90	33.30
Wards fayalite	50.90(39)	50.02	49.67	49.91
Rockport fayalite	52.29(26)	52.03	52.07	51.52
Synthetic fayalite	54.55(33)	52.18	52.56	53.17
Fe metal	100.0	99.61	99.61	99.56

Notes: The results were obtained at 7 kV and 90 nA with the SX51 microprobe and three WDS. Numbers in parentheses are the estimated standard deviations (uncertainties on the last digits).

method, but it gives slightly less accurate quantitative results. The mean RSD (in absolute value and in percent) of the Fe data obtained on the SXFiveFE instrument is 1.58 and 2.63% when using the area k-ratio calibration curve and the peak maximum k-ratio calibration curve, respectively. The mean RSD for the SX51 instrument is almost identical for both methods (3.60 and 3.61% using the area k-ratio and peak maximum k-ratio calibration curves, respectively). The compromise in accuracy relative to the speed of acquisition may be acceptable for certain applications.

IMPLICATIONS

The discovery that a simple calibration curve approach, employing the relatively high-intensity Fe*L*α and *L*β peak integrals, can be used as a platform-independent tool for low-kV quantitative analysis is significant. It provides an easy-to-use method to quantify the Fe *L* X-ray signal by applying a universal equation and utilizing an easily available standard material like pure iron metal. The only drawback, longer acquisition of one or multiple wavescans (we recommend averaging of 2 or 3), is balanced by the significantly higher count rates relative to those of the Fe*L*ℓ line, thereby reducing the analytical statistical error.

While applying the calibration curve approach to only the net Fe*L*α peak maximum intensities improves ease and speed of acquisition, it requires re-evaluating the calibration curve for each spectrometer and requires having a set of olivine samples of known composition with Fe content covering the concentration range of interest.

Our technique is particularly suited to high-spectral resolution, parallel channel X-ray detectors such as the SXES as they acquire the entire Fe *L* X-ray spectrum simultaneously. While their presence in laboratories is currently very sparse, they could play a more important role in the future, particularly for geoscientists.

Future lines of research may include investigating the robustness of the calibration curve approach at different accelerating voltages (e.g., 3, 5, and 10 kV) and different spectrometer takeoff angles. In addition, the exploration of other iron-rich systems (minerals and glasses) could determine whether their Fe*L*α+*L*β area k-ratio might fall on the same curve, or different curves, or have no correlation with composition.

It may also be of interest to try to obtain the same calibration curve with an EDS as it should work if the takeoff angle is 40° and would expand the applicability of this quantification method to a wider audience.

ACKNOWLEDGMENTS AND FUNDING

We thank the following for providing a second set of olivines for testing the calibration curve: Noriko Kita, Mike Spicuzza, and Kohei Fukuda. The authors thank the two reviewers for their detailed comments which helped make the manuscript more complete. Support for this research came from the National Science Foundation: EAR13-37156 (J.H.F.), EAR15-54269 (J.H.F.), and EAR-1625422 (A.V.D.H.).

REFERENCES CITED

Anderson, C.A. (1967) The quality of X-ray microanalysis in the ultra-soft X-ray region. British Journal of Applied Physics, 18, 1033–1043.

Anderson, C.A., and Hasler, M.F. (1966) Extension of electron microprobe techniques to biochemistry by the use of long wavelength X-rays. In R. Castaing, P. Deschamps, and J. Philibert, Eds., Proceedings of the Fourth International Conference on X-ray Optics and Microanalysis, p. 310–327. Hermann, Paris.

Barker, F., Wones, D.R., Sharp, W.N., and Desborough, G.A. (1975) The Pikes Peak batholith, Colorado Front Range, and a model for the origin of the gabbro–anorthosite–syenite–potassic granite suite. Precambrian Research, 2, 97–160.

Barkshire, I., Karduck, P., Rehbach, W.P., and Richter, S. (2000) High-spatial-resolution low-energy electron beam X-ray microanalysis. Microchimica Acta, 132, 113–128.

Bence, A.E., and Albee, A.L. (1968) Empirical correction factors for the electron microanalysis of silicates and oxides. Journal of Geology, 76(4), 382–403.

Bertin, E.P. (1975) Principles and Practice of X-ray Spectrometric Analysis, 1079 p. Plenum Press.

Buse, B., and Kearns, S. (2015) Importance of carbon contamination in high-resolution (FEG) EPMA of silicate minerals. Microscopy and Microanalysis. 21, 594–605. doi:10.1017/S1431927615000288.

——— (2018) Quantification of olivine using Fe Lα in electron probe microanalysis (EPMA). Microscopy and Microanalysis. 24, 1–7. doi: 10.1017/S1431927618000041.

Castaing, R. (1952) Application des sondes électroniques à une méthode d'analyse ponctuelle chimique et cristallographique. Ph.D. thesis, Université de Paris, France. (Publication ONERA no. 55)

——— (1955) Application of Electron Probes to Local Chemical and Crystallographic Analysis (Application des sondes électroniques à une méthode d'analyse ponctuelle chimique et cristallographique). Translation by Pol Duwez and David B. Wittry, California Institute of Technology. (http://www.microprobe.org/history/Castaing-Thesis-clearscan.pdf/view)

——— (1960) Electron probe microanalysis. In M. Marton, Ed., Advances in Electronics and Electron Physics, p. 317–386. Academic.

Castaing, R., and Fredriksson, K. (1958) Analyses of cosmic spherules with an X-ray microanalyser. Geochimica et Cosmochimica Acta, 14, 114–117.

Donovan, J., Kremser, D., Fournelle, J., and Goemann, K. (2018) Probe for Windows User's Guide and Reference, Enterprise Edition. Probe Software, Inc., Eugene, Oregon.

Duncumb, P. (1960) Improved resolution with X-ray scanning microanalyser. In A. Engstrom, V. Cosslett, and H. Pattee, Eds., X-ray Microscopy and X-ray Microanalysis, Proceedings of 2nd International Symposium, 365–371. Elsevier, Amsterdam.

Fialin, M., Wagner, C., and Pascal, M.-L. (2011) Iron speciation using electron microprobe techniques: application to glassy melt pockets within a spinel lherzolite xenolith. Mineralogical Magazine, 75, 347–362.

Finch, C.B., Clark, G.W., and Kopp, O.C. (1980) Czochralski growth of single-crystal fayalite under controlled oxygen fugacity conditions. American Mineralogist, 65, 381–389.

Fournelle, J.H. (1988) The geology and petrology of Shishaldin Volcano, Unimak Island, Aleutian Islands. Ph.D. thesis, Johns Hopkins University, Baltimore.

Fournelle, J., Cathey, H., Pinard, P.T., and Richter, S. (2016) Low voltage EPMA: experiments on a new frontier in microanalysis—analytical lateral resolution. In IOP Conference Series: Materials Science and Engineering, 109, 1, 012003. IOP Publishing.

Gopon, P., Fournelle, J., Sobol, P.E., and Llovet, X. (2013) Low-voltage electron-probe microanalysis of Fe–Si compounds using soft X-rays. Microscopy and Microanalysis, 19, 1698–1708.

Heinrich, K.F.J. (1987) Mass absorption coefficients for electron probe microanalysis. In J.D. Brown and R.H. Packwood, Eds., Proceedings of the 11th international Congress on X-ray Optics and Microanalysis, 67–119. University of Western Ontario Press, London, Ontario.

Hovington, P., Drouin, D., and Gauvin, R. (1997a) CASINO: A new Monte Carlo code in C language for electron beam interaction—Part I: Description of the program. Scanning, 19, 1–14.

Hovington, P., Drouin, D., Gauvin, R., and Joy, D.C. (1997b) Parameterization of the range of electrons at low energy using the CASINO Monte Carlo program. Microscopy and Microanalysis, 3, 885–886.

International Organization for Standardization (2003) Microbeam analysis—Electron probe microanalysis—Guidelines for the determination of experimental parameters for wavelength dispersive spectroscopy. ISO 14594.

Jarosewich, E., Nelen, J.A., and Norberg, J.A. (1980) Reference samples for electron microprobe analysis. Geostandards Newsletter, 4(1), 43–47.

Kearns, S., Buse, B., and Wade, J. (2014) Mitigating thermal beam damage with metallic coats in low voltage FEG-EPMA of geological materials. Microscopy and Microanalysis, 20(S3), 740–741.

Keil, K., and Fredriksson, K. (1964) The iron, magnesium, and calcium distribution in coexisting olivines and rhombic pyroxenes of chondrites. Journal of Geophysical Research, 69(16), 3487–3515.

Li, X., Zhang, C., Almeev, R.R., Zhang, X.-C., Zhao, X.-F., Wang, L.-X., Koepke, J., and Holtz, F. (2019) Electron probe microanalysis of $Fe^{2+}/\Sigma Fe$ ratios in calcic and sodic-calcic amphibole and biotite using the flank method. Chemical Geology, 509, 152–162.

Libourel, G., and Portail, M. (2018) Chondrules as direct thermochemical sensors of solar protoplanetary disk gas. Science Advances, 4(7), p.eaar3321.

Llovet, X., and Galan, G. (2003) Correction of secondary X-ray fluorescence near grain boundaries in electron microprobe analysis: Application to thermobarometry of spinel lherzolites. American Mineralogist, 88, 121–130.

Llovet, X., and Salvat, F. (2016) PENEPMA: a Monte Carlo programme for the simulation of X-ray emission in EPMA. In IOP Conference Series: Materials Science and Engineering, 109, 1, 012009. IOP Publishing.

Llovet, X., Heikinheimo, E., Galindo, A.N., Merlet, C., Bello, J.A., Richter, S., Fournelle, J., and Van Hoek, C.J.G. (2012) An inter-laboratory comparison of EPMA analysis of alloy steel at low voltage. In IOP Conference Series: Materials Science and Engineering, 32, 1, 012014. IOP Publishing.

Llovet, X., Pinard, P.T., Heikinheimo, E., Louhenkilpi, S., and Richter, S. (2016) Electron probe microanalysis of Ni silicides using Ni-L X-ray lines. Microscopy and Microanalysis, 22, 1233–1243.

McSwiggen, P. (2014) Characterisation of sub-micrometre features with the FE-EPMA. In IOP Conference Series: Materials Science and Engineering, 55, 1, 012009. IOP Publishing.

Merlet, C., and Llovet, X. (2012) Uncertainty and capability of quantitative EPMA at low voltage—A review. In IOP Conference Series: Materials Science and Engineering, 32, 1, 012016. IOP Publishing.

Moy, A., Fournelle, J.H., and von der Handt, A. (2019) Quantitative measurement of iron-silicides by EPMA using the Fe Lα and Lβ X-ray lines: a new twist to an old approach. Microscopy and Microanalysis, 25, 664–674. doi: 10.1017/S1431927619000436

Pinard, P.T., and Richter, S. (2016) Quantification of low concentration elements using soft X-rays at high spatial resolution. In IOP Conference Series: Materials Science and Engineering, 109, 1, 012013. IOP Publishing

Pouchou, J.L. (1996) Use of soft X-rays in microanalysis. Mikrochimica Acta 13(Suppl.), 39–60.

Pouchou, J.L., and Pichoir, F. (1991) Quantitative analysis of homogeneous or stratified microvolumes applying the model "PAP", In K.F.J. Heinrich and D.E. Newbury, Eds., Electron Probe Quantitation, p. 31–75. Plenum Press.

Reed, S.J.B. (1966) Spatial resolution in electron probe microanalysis. In R. Castaing, P. Deschamps, and J. Philibert, Eds., Proceedings of the Fourth International Conference on X-ray Optics and Microanalysis, p. 339–349. Hermann, Paris.

Rémond, G., Myklebust, R., Fialin, M., Nockolds, C., Phillips, M., and Roques-Carmes, C. (2002) Decomposition of wavelength dispersive X-ray spectra. Journal of Research of the National Institute of Standards and Technology, 107, 509–529.

Ritchie, N.W. (2011) Getting Started with NIST DTSA-II. Microscopy Today, 19(1), 26–31.

Rose, T. R., Sorensen, S.S., and Post, J.E. (2009) The impurities in the Rockport fayalite microbeam standard: How bad are they? American Geophysical Union, Fall Meeting 2009, abstract V31E-2008.

Salvat, F., Fernandez Varea, J.M., and Sempau, J. (2013) PENELOPE—A code system for Monte Carlo simulation of electron and photon transport. OECD/Nuclear Energy Agency, Issy-les-Moulineaux, France.

Saunders, K., Buse, B., Kilburn, M.R., Kearns, S., and Blundy, J. (2014) Nanoscale characterisation of crystal zoning. Chemical Geology, 364, 20–32.

Shea, T., Lynn, K.J., and Garcia, M.O. (2015) Cracking the olivine zoning code: Distinguishing between crystal growth and diffusion. Geology, 43, 935–938. doi: 10.1130/G37082.1.

Terauchi, M., and Sato, Y. (2018) Chemical state analyses by soft X-ray emission spectroscopy. JEOL NEWS, 53(1), 30–35.

Terauchi, M., Takahashi, H., Handa, N., Murano, T., Koike, M., Kawachi, T., Imazono, T., Hasagawa, N., Koeda, M., Nagano, T., and Sasai, H. (2011) An extension up to 4 keV by a newly developed multilayer-coated grating for TEM-SXES spectrometer. Microscopy and Microanalysis, 17(S2), 604–605.

Vladár, A.E., and Postek, M.T. (2009) The scanning electron microscope. In J. Orloff, Ed., Handbook of Charged Particle Optics, 2nd ed., p. 437–496. CRC Press.

Ziebold, T.O., and Ogilvie, R.E. (1963) Quantitative analysis with the electron microanalyzer. Analytical Chemistry, 35(6), 621–627.

Zschornack, G.H. (2007) Handbook of X-Ray Data. Springer-Verlag.

Manuscript received October 30, 2018
Manuscript accepted April 26, 2019
Manuscript handled by Sasa Bajt

Endnote:

[1] The physical terms kV and keV are used here in the strict sense: kV refers to an electrical potential (as between the cathode and anode of the source), whereas keV refers to an energy of a "particle" such as an electron or photon.

[2] Deposit item AM-19-86865, Supplemental Figures and Tables. Deposit items are free to all readers and found on the MSA website, via the specific issue's Table of Contents (go to http://www.minsocam.org/MSA/AmMin/TOC/2019/Aug2019_data/Aug2019_data.html).